Journal of
Materials Chemistry C

ROYAL SOCIETY
OF CHEMISTRY

PAPER

View Article Online
View Journal | View Issue

Cite this: *J. Mater. Chem. C*, 2024, **12**, 4417

Received 24th December 2023,
Accepted 19th February 2024

DOI: 10.1039/d3tc04759h

rsc.li/materials-c

Strain-induced tunable valley polarization and topological phase transition in SVSiN$_2$ monolayer†

Yunxi Qi,[a] Can Yao,[a] Jun Zhao *[a] and Hui Zeng *[b]

The potential application of a two-dimensional (2D) ferrovalley semiconductor in the field of valleytronics has sparked extensive research interest. Using first-principles calculations, we predict that the SVSiN$_2$ monolayer is a promising ferrovalley material with excellent dynamical and thermal stability, and its Curie temperature is around room temperature. A giant valley polarization of −72.73 meV is obtained by shifting the magnetization direction from in-plane to out-of-plane. The valley-contrasting properties of the SVSiN$_2$ monolayer can be remarkably modulated by in-plane strains. Most importantly, topological phase transition is predicted to be realized by a 5.5–6% tensile strain, which is verified by the nonzero Chern number and the nontrivial edge state. Compared to the in-plane strain modulation, the valley-dependent properties of the SVSiN$_2$ monolayer are robust to vertical electric fields. Our findings could enrich the physical understanding of the effects of manipulating the valley-dependent properties of 2D ferrovalley semiconductors, facilitating potential applications of 2D Janus monolayers for valleytronics.

1 Introduction

A valley, which is defined as a local extremum in momentum space, can be used to manipulate information encoding, transfer, and processing.[1] Correspondingly, valleytronics that relying on manipulating the emergent degree of freedom of a valley, has received increasing research focus in recent years.[2] However, valleys may degenerate in terms of energy aspect due to the protection of time reversal symmetry. As a result, breaking the degeneracy of valleys is crucial for fabricating high-storage density and low-energy electronic devices.[3] Over the past decade, the 2D transition metal dichalcogenides (TMDs) monolayer with broken inversion symmetry and spin–orbit coupling (SOC) has extensively promoted the development of valleytronics.[4–7] Non-equilibrium distributions for valley carriers in TMDs can be realized by many routes, including the valley contrasting optical selection rule, the Zeeman effect of the external magnetic field, magnetic atom doping, and magnetic proximity effect.[6–11] However, some drawbacks are accompanied with the implementation of these routes. For example, the optical pumping method demands harsh experimental conditions. The efficiency of valley polarization generated by an external magnetic field is very low. Regarding magnetic atom doping, it may lead to unstable valley polarization as a result of introducing impurity scattering between different valleys. Fortunately, the 2D intrinsic ferrovalley materials provide new opportunities to solve these issues. Therefore, it is necessary to explore novel intrinsic ferrovalley semiconductors (FVS) with emerging valley-related properties.

Monolayered FVS exhibit not only spontaneous valley polarization, but also valley-contrasting transport under the optical selection rule resulting from spin-valley coupling. This is attributed to the presence of inherent long-range ferromagnetism combined with the SOC effect, and furthermore, the ferromagnetism is crucial because it breaks the time-reversal symmetry of the system.[12,13] In addition, some emergent quantum states, such as topological states and half-valley-metal (HVM) states, are predicted to be achievable using a finite strain on the FVS material.[14,15] However, only a few 2D materials are shown to exhibit spontaneous valley polarization, such as the monolayers of 2H-VSe$_2$,[16] Nb$_3$I$_8$,[17] NbX$_2$,[18] and GdI$_2$.[19] Moreover, most 2D monolayers under consideration essentially possess an in-plane easy magnetization axis. In contrast, the FVS materials with tunable multiple valley states and out-of-plane magnetization are rarely reported.[20] Correspondingly, searching for a new intrinsic FVS materials is of great importance to broaden the practical application of the valleytronics.[21]

To date, most intrinsic FVS materials are synthesized or proposed on the basis of binary or ternary chemical compounds.[22–27] In recent years, layered 2D materials MoSi$_2$N$_4$ and WSi$_2$N$_4$ have been prepared through chemical vapor deposition (CVD).[28] Many theoretical investigations are devoted

---

[a] *New Energy Technology Engineering Laboratory of Jiangsu Province & School of Science, Nanjing University of Posts and Telecommunications, Nanjing, Jiangsu 210023, China. E-mail: zhaojun@njupt.edu.cn*

[b] *School of Microelectronics, Nanjing University of Science and Technology, Nanjing, Jiangsu 210094, China. E-mail: zenghui@njust.edu.cn*

† Electronic supplementary information (ESI) available. See DOI: **https://doi.org/10.1039/d3tc04759h**

to the understanding of MA_2Z_4 (M = Cr, Mo, W, V, Nb, Ta, Ti, Zr or Hf; A = Si or Ge; and Z = N, P, As) based 2D materials, using first principles calculations. The MA_2Z_4 family has emerging topological, magnetic, valley, superconducting, and catalytic properties.[29–34] Hence, the physical properties of various MA_2Z_4-based van der Waals (vdW) heterostructures have also been investigated to explore their electronic and optoelectronic applications.[35,36]

In this work, we propose a Janus $SVSiN_2$ monolayer with five layers of atoms, which can be obtained from the VSi_2N_4 monolayer by replacing one side of the N–Si–N atom with an S atom. It can be regarded as a 2D Janus material with reflection symmetry breaking.[37] The $SVSiN_2$ monolayer is predicted to be a FVS material with a Curie temperature of 260 K. It has excellent thermal and dynamical stability. We predict that a large valley polarization of −72.73 meV can be achieved by switching the magnetization direction of the $SVSiN_2$ monolayer from the in-plane direction to the out-of-plane direction. A tight-binding model is used to elucidate the anomalous valley Hall effect (AVHE) induced by the valley polarization and the opposite Berry curvatures at the $K/-K$ valleys in the $SVSiN_2$ monolayer. Strain and electric field are also introduced to tune the valley polarization and Berry curvature of the system. Most importantly, a biaxial tensile strain of 5.5–6% can induce valley quantum anomalous Hall effect. Our findings broaden the knowledge of 2D ferrovalley materials and deepen the understanding of strain-induced topological and valley states in the Janus $SVSiN_2$ monolayer.[38–41]

2 Computational methods

All our first-principles calculations are based on density functional theory (DFT) implemented using the Vienna *ab initio* simulation package (VASP).[42,43] The Perdew–Burke–Ernzerhof (PBE) exchange–correlation function of the generalized gradient approximation (GGA) was utilized to calculate the structural relaxation and electronic structure.[44] We use the GGA+U method to describe the strong correlation correction of V-3d orbitals. We test various U-values and compare them with the electronic structures obtained from the hybrid functional HSE06,[45] which typically gives an accurate electronic structure. It is found that the calculated results obtained from GGA+U and HSE06 agree well when U_{eff} = 3.2 eV. To avoid interlayer interactions, a vacuum layer of 20 Å is considered along the z-axis direction. The cutoff energy is 500 eV for the plane-wave basis. To fully optimize the structure, the convergence criteria for total energy and atomic residual force are 1×10^{-8} eV and 0.001 eV Å^{-1}, respectively. The first Brillouin zone integration is carried out using 16 × 16 × 1 Γ-centered k-grids.[46] The 9 × 16 × 1 Monkhorst–Pack k-meshes are used to calculate ferromagnetic (FM)/antiferromagnetic (AFM) energy using rectangular superlattices. Table S1 (ESI†) shows that the effects of dipole correction on the geometric structure and electronic property are negligible. The calculations regarding the $SVSiN_2$ monolayer will not consider the dipole correction hereafter. The SOC effect is considered to study the magnetocrystalline anisotropy and electronic properties of the $SVSiN_2$ monolayer. The phonon dispersion of a 4 × 4 × 1 supercell is calculated using density functional perturbation theory and PHONOPY code.[47] The *ab initio* molecular dynamics (AIMD) simulations were carried out using a 4 × 4 × 1 supercell at 300 K. The VASPBERRY subroutine is used to calculate the materials' Berry curvature and circular polarization.[48] In addition, we construct the maximum localized Wannier function (MLWF) using the WANNIER90 package,[49] and calculate the edge states and anomalous Hall conductivity with the help of WANNIERTOOLS subroutine.[50] Based on the Heisenberg model, we perform Monte Carlo (MC) simulations on a 10 × 10 × 1 supercell using the multi-dimensional Curie Temperature Simulation Package.[51] All crystal structures are visualized by VESTA software.[52]

3 Results and discussion

3.1 Atomic structure and stability

We first study the atomic and electronic structures of $SVSiN_2$, as shown in Fig. 1(a) and (b). The stacking order of the $SVSiN_2$ monolayer is S–V–N–Si–N, which can be considered to be a Janus structure. The lattice constant of the $SVSiN_2$ monolayer is $a = b = 2.952$ Å. The crystal symmetry of the $SVSiN_2$ monolayer is C_{3v}. Similar to the TMDs, the inversion symmetry of the $SVSiN_2$ monolayer is also broken. We conduct AIMD simulations to explore the thermal stability of the $SVSiN_2$ monolayer, as illustrated in Fig. 2(a).

During a simulation time of 5 ps, the simulated results show that the total energy fluctuation is not significant, and is always near the equilibrium value at a temperature of 300 K. As shown in the inset of Fig. 2(a), there is no significant structural break in the final snapshot of the $SVSiN_2$ monolayer. The calculated AIMD result indicates that the $SVSiN_2$ monolayer possesses excellent thermal stability at room temperature. The phonon dispersion shown in Fig. 2(b) illustrates that there is no imaginary frequency in any branches, ensuring the dynamical stability of the $SVSiN_2$ monolayer. The structural stability is

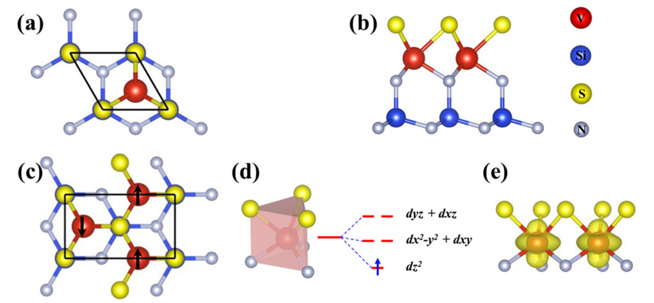

Fig. 1 Top- (a) and side-views (b) of the primitive structure of the $SVSiN_2$ monolayer. (c) The top view of a rectangular supercell for magnetic ground state calculations. For the AFM configuration, the spin directions are marked with black arrows. (d) A schematic diagram of the d-orbital energy levels of the V ion in a trigonal prismatic crystal field, and (e) shows the spin density distribution of the $SVSiN_2$ monolayer.

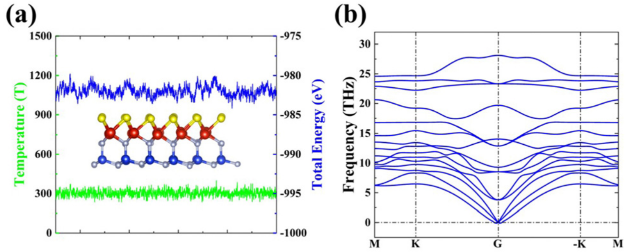

Fig. 2 (a) AIMD calculation and (b) phonon spectrum of the $SVSiN_2$ monolayer.

evaluated by its formation energy (E_{form}), which is defined as:

$$E_{\text{form}} = \frac{E_{\text{total}} - E_t(\text{S}) - E_t(\text{V}) - E_t(\text{Si}) - 2E_t(\text{N})}{N} \quad (1)$$

where E_{total} is the total energy of the $SVSiN_2$ monolayer, and E_t is the energy of each constituent element in their standard state (per atom). The calculated formation energy of the $SVSiN_2$ monolayer is −0.93 eV per atom, which is very close to the corresponding value (−0.96 eV per atom) reported previously for the $SMoSiN_2$ monolayer.[53] The negative formation energy indicates the possible experimental feasibility of the 2D monolayer. Therefore, the $SVSiN_2$ monolayer is predicated to be more feasible in experimental fabrication compared to the $SeMoSiN_2$ (E_{form} = −0.77 eV per atom) and $TeMoSiN_2$ (E_{form} = −0.46 eV per atom) monolayers.[53]

3.2 Magnetic ground state

We investigate the electron occupancy in V atoms based on crystal field theory. In a trigonal prismatic crystal field environment, the V-d orbitals split into a low-lying d_{z^2} orbital, followed by (d_{xy}, $d_{x^2-y^2}$) and (d_{xz}, d_{yz}) orbitals. Among them, an unpaired electron occupies the d_{z^2} orbital, which is evidenced by the spin density distribution of the occupied V-d orbital exhibited in Fig. 1(d) and (e), which generates a net magnetic moment of $1\mu_B$ into the $SVSiN_2$ monolayer. In Fig. S1(a) (ESI†), we evaluate the effects of different U_{eff} values on the magnetic moments of the V atom. The calculated results show that the atomic magnetic moments obtained are in the range 2–4 eV, which agrees well with the theoretical values. The average distance between two V atoms in the $SVSiN_2$ is 2.952 Å. Such a large atomic distance results in a weak direct exchange interaction force between the V atoms. And the super-exchange mechanism is considered to dominate the interaction between V atoms since the V–N–V angle is close to 90°. According to the Goodenough–Kanamori rule,[54,55] the $SVSiN_2$ monolayer adopts FM-ordered ground states and forms FM coupling, which is attributed to the overlap of V-d_{z^2} and N-p orbitals.

We also calculate the energy difference (Δ_E) with respect to different U_{eff} values between the AFM- and FM-ordered states by $\Delta_E = E_{\text{AFM}} - E_{\text{FM}}$, as presented in Fig. S1(b) (ESI†). The rectangular supercell shown in Fig. 1(c) is employed for the Δ_E calculation. The results indicate that the $SVSiN_2$ monolayer remains in the FM ground state with the U_{eff} value changing within the range 0–5 eV. Compared to the calculated Δ_E results under different U_{eff} with the corresponding HSE06 results, we find that two calculations agree well when U_{eff} = 3.2 eV. The calculated local magnetic moment of the system in Fig. S1(a) (ESI†) is about $1.044\mu_B$ with U_{eff} = 3.2 eV, which is consistent with the above analysis in Fig. 1(d). Moreover, the band structures of the $SVSiN_2$ monolayer under different U_{eff} values is shown in Fig. S2 (ESI†). It can be seen that the $SVSiN_2$ is a half-metal when U_{eff} = 0 eV. When the U_{eff} value changes in the range 3–4 eV, the band structure of the $SVSiN_2$ monolayer is qualitatively consistent with that obtained from HSE06. In addition, the projected density of states shown in Fig. S3 (ESI†) demonstrates that there is no significant difference in orbital contributions between PBE+U and HSE06. Therefore, in the following discussion, we choose U_{eff} = 3.2 eV to investigate the spin valley coupling of the $SVSiN_2$ monolayer.

When the SOC effect is considered, the direction of susceptibility depends on the area where the electron clouds overlap, which can be described by the magnetic anisotropy energy (E_{MAE}) and is calculated by:

$$E_{\text{MAE}} = E_{\text{MCA}} + E_{\text{MSA}} \quad (2)$$

where E_{MCA} and E_{MSA} refer to the magnetic crystal anisotropy energy and magnetic shape anisotropy energy, respectively. The E_{MCA} is attributed to the SOC effect, and it is defined as:

$$E_{\text{MCA}} = E_{[100]} - E_{[001]} \quad (3)$$

where $E_{[100]}$ ($E_{[001]}$) represent the total energy of the $SVSiN_2$ monolayer with an in-plane (out-of-plane) magnetic moment.[56] The E_{MSA} is contributed by the dipole–dipole (D–D) interaction, which tends to make the direction of spin parallel to the monolayer.[57] The D–D interaction can be defined as:

$$E_{\text{D-D}} = \frac{\mu_0}{8\pi}\sum_{i\neq j}\frac{1}{r_{ij}^{3}}\left[\vec{\mathbf{M}}_i\cdot\vec{\mathbf{M}}_j - \frac{3}{r_{ij}^{2}}\left(\vec{\mathbf{M}}_i\cdot\vec{\mathbf{r}}_{ij}\right)\left(\vec{\mathbf{M}}_j\cdot\vec{\mathbf{r}}_{ij}\right)\right] \quad (4)$$

where $\vec{M}_i$ represents the magnetic moment of the V atom at position i, and $\vec{r}_{ij}$ represents the vector of V atoms at positions i and j. Correspondingly, E_{MSA} can be expressed as:

$$E_{\text{MSA}} = E^{[100]}_{\text{D-D}} - E^{[001]}_{\text{D-D}} = \frac{3}{2}\frac{\mu_0 M^2}{4\pi}\sum_{i\neq j}\frac{1}{r_{ij}^{3}}\cos^2\theta_{ij} \quad (5)$$

where θ_{ij} is the angle between $\vec{M}_i$ and $\vec{r}_{ij}$. The E_{MCA} values calculated at different k-meshes are plotted in Fig. S4 (ESI†). It is noted that the E_{MCA} results are almost unchanged when the k-meshes are increased from 16 × 16 × 1 to 28 × 28 × 1, indicating that a converged result is obtained. The E_{MAE} is predicted to be −93.08 μeV with E_{MCA} = −75.88 μeV and E_{MSA} = −17.20 μeV. Our calculated value of E_{MSA} agrees well with E_{MSA} = −17 μeV reported in the case of the monolayered $VSiGeN_4$.[58] It is noticed that the calculated E_{MSA} values are approximately −14 to −17 μeV for $VSiGeN_4$ (−16 μeV) and $VSiSnN_4$ (−14 μeV) and VSi_2N_4 (−17 μeV) monolayers,[59] suggesting that the D–D interaction between the V atoms are very similar. In contrast, the E_{MCA} is defined as the energy difference between the in-plane (x-direction) spin configuration and out-of-plane (z-direction) spin configuration. Our calculated E_{MSA}

indicates that the SOC effect makes the $SVSiN_2$ monolayer have in-plane spin configuration, which is more prominent than that in the VSi_2N_4 monolayer (E_{MCA} = −42 to −64 μeV).[29,59] Moreover, we calculated the influence of different U_{eff} values on E_{MCA}. With the enhancement of the Coulomb repulsion effect, it is expected to induce the spin configuration of the $SVSiN_2$ monolayer to shift from an in-plane to out-of-plane direction. This anticipation is confirmed by Fig. S5 (ESI†). The calculated E_{MCA} is found to change to a positive value when U_{eff} = 5 eV. Hence, the negative E_{MAE} means that the magnetization axis of the $SVSiN_2$ monolayer is parallel to the plane of the monolayer, revealing that the $SVSiN_2$ monolayer is a 2D *XY* magnet.[60,61] In principle, the magnetization orientation of the $SVSiN_2$ monolayer can be elaborately modulated from the in-plane direction to the out-of-plane direction by overcoming a 93.08 μeV energy barrier. Furthermore, the negative E_{MAE} is also obtained in the 2D VSi_2N_4 and Janus $VSiGeN_4$ and $VSiSnN_4$ monolayers.[59]

To further explore the nature of the in-plane E_{MAE}, we calculate the orbital contribution of the V atom to the E_{MCA}, as shown in Fig. S6 (ESI†). For V-d orbitals, the in-plane E_{MCA} is mainly contributed by hybridization of $d_{xy}/d_{x^2-y^2}$, d_{z^2}/d_{yz}, and d_{z^2}/d_{xz}. However, the E_{MCA} contribution of the V atom in the V-p orbital is one order of magnitude greater than that in the V-d orbital. Therefore, the in-plane E_{MAE} mainly originates from the hybridization of the p-orbitals. The Curie temperature (T_c) of the $SVSiN_2$ monolayer is estimated on the basis of the Heisenberg model:

$$H = -\sum_{\langle ij \rangle} J_{ij} S_i \cdot S_j - D\left(S_i^z\right)^2 \tag{6}$$

where S_i is the spin operator (S = 1/2), J_{ij} is the strength of the exchange interaction between site i and j, and D is the single-ion anisotropy constant. Our DFT calculations extrapolate J = 65.5 meV and D = 93.08 μeV. We also perform MC simulations which predict a T_c of about 260 K, as shown in Fig. 3. The $SVSiN_2$ monolayer has a higher T_c than that of the CrX_3 (X = F, Cl, Br, I) monolayer,[62] which is desirable for the practical application of valleytronics.

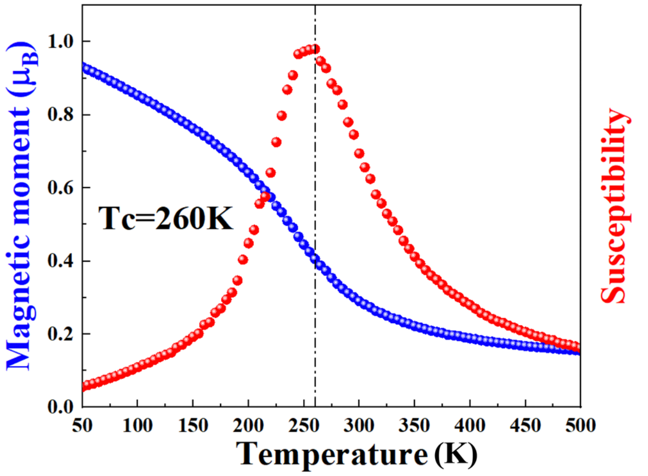

Fig. 3 The Curie temperature of the $SVSiN_2$ monolayer based on Monte Carlo simulations.

3.3 Electronic structure

The band structure of the $SVSiN_2$ monolayer is shown in Fig. 4. When the SOC is not considered, the electronic bands are completely spin polarized, as shown in Fig. 4(a). The valence band maximum (VBM) and conduction band minimum (CBM) of the $SVSiN_2$ monolayer is located at the *G* and *M* point, respectively, leading to an indirect bandgap of about 0.53 eV. We define the valley splitting of the valence band Δ_{VB} (conduction band Δ_{CB}) as:

$$\Delta_{VB} = E_K^{VB} - \mathrm{E}_{-K}^{VB}(\Delta_{CB} = E_K^{CB} - E_{-K}^{CB}) \tag{7}$$

where E_K^{VB} and E_K^{CB} (E_{-K}^{VB} and E_{-K}^{CB}) denote the energy extremum of the *K* (−*K*) valley valence and conduction band, respectively. It is found that the valley-dependent electronic states are fully spin polarized, *i.e.*, both the CBM and VBM at the *K*/−*K* valleys have a contributing up-spin component. The valley polarization is protected by time-reversal symmetry, and the in-plane magnetization does not break such symmetry. Therefore, valley splittings for the valence band Δ_{VB} and for the conduction band Δ_{VB} are absent when the magnetization axis is along the +*x* direction, as confirmed in Fig. 4(b). In contrast, the time-reversal symmetry is broken when the magnetization axis is along the out-of-plane direction, leading to a prominent Δ_{VB} of about −72.73 meV as shown in Fig. 4(c). The conduction band splitting is small and is predicted to be a mere 4.32 meV. When the magnetization direction is reversed to the −*z* direction, the valley splitting of the Δ_{VB} (Δ_{CB}) is 72.73 (−4.32) meV, as presented in Fig. 4(d). Notably, the up-spin component at the *K*/−*K* valleys is fully polarized when the magnetization direction is in the +*z* direction, and the −*z* magnetization direction will flip the full polarization to the down-spin component at the *K*/−*K* valleys.[29] For the $SVSiN_2$ monolayer, the +*z* (−*z*) directed magnetization selectively stimulates the hole carrier at the −*K*

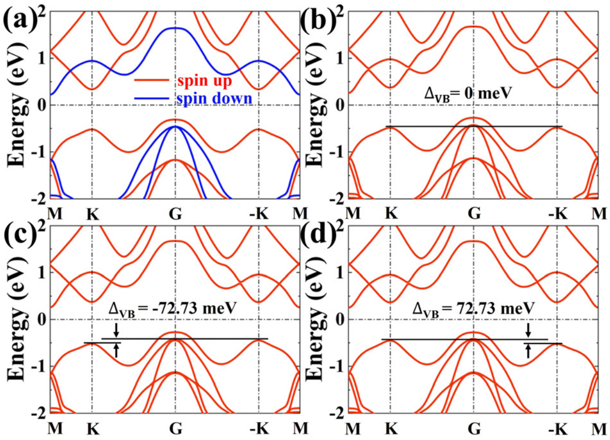

Fig. 4 (a) The band structure of the $SVSiN_2$ monolayer without SOC. (b)–(d) The band structure of the $SVSiN_2$ monolayer with SOC, where (b)–(d) represent the magnetic moment of V ions in the +*x*, +*z*, and −*z* directions, respectively.

(K) valley-coupled with up (down) spin polarization, as shown in Fig. 4(c) and (d), respectively. As a consequence, both spin and valley are locked with the magnetization direction. This phenomenon is also observed in the RuClBr monolayer.[63] It provides the possibility to switch opposite spin polarizations at the K/$-K$ valleys by intentionally manipulating the magnetization direction of the SVSiN$_2$ monolayer. Similar valley polarization phenomena are also obtained in the MoSi$_2$N$_4$/CrI$_3$ and MoTe$_2$/MnSe$_2$ heterostructures resulting from the magnetic proximity effect.[64,65] Moreover, such spin polarization at the K/$-K$ valleys is completely different from the spin-valley locking in the MoS$_2$ monolayer, where the K/$-K$ valleys are simultaneously coupled with up/down spins, respectively.[66]

To further examine the characteristics of valley splitting in the SVSiN$_2$ monolayer, we derive a simple model to describe the intensity of valley splitting for the SVSiN$_2$ monolayer:[67]

$$\begin{aligned}\hat{H}_{\rm soc} &= \alpha\hat{L}\cdot\hat{S}\\ &= \lambda\left(\hat{L}_z\cos\theta+\frac{1}{2}\hat{L}_+{\rm e}^{-{\rm i}\phi}\sin\theta+\frac{1}{2}\hat{L}_-{\rm e}^{+{\rm i}\phi}\sin\theta\right)\end{aligned} \tag{8}$$

where λ is the coupling strength of the SOC. Based on Fig. 4(a), we find that both valence band and conduction band at the K/$-K$ valley are contributed by the spin-up electronic states. Therefore, this model only considers interactions between the same spin states. According to Fig. 5(a), the valence band valley of the K/$-K$ point is mainly contributed by the $d_{xy}/d_{x^2-y^2}$, and the conduction band valley is governed by d_{z^2}. Therefore, the basis function of the valence band valley (conduction band valley) can be described as:

$$|\psi_{\rm v}^{\tau}\rangle=\frac{1}{\sqrt{2}}\left(|d_{x^2-y^2}\rangle+i\tau|d_{xy}\rangle\right)\quad(|\psi_{\rm c}\rangle=|d_{z^2}\rangle) \tag{9}$$

where τ is the valley index and equals 1 (-1) at the K ($-K$) valley. Hence, when the magnetization direction is parallel to the z-axis, the matrix elements of the SOC operator $\hat{L}\cdot\hat{S}$ are based on d-orbitals.[68] The valence band (conduction band) valley splitting can be expressed as:

$$\Delta_{\rm CB}=\langle d_{z^2}|\hat{H}_{\rm soc}|d_{z^2}\rangle-\langle d_{z^2}|\hat{H}_{\rm soc}|d_{z^2}\rangle=0 \tag{10}$$

$$\begin{aligned}\Delta_{\rm VB}&=\langle\psi_{\rm v}{}^{1}|\hat{H}_{\rm soc}|\psi_{\rm v}{}^{1}\rangle-\langle\psi_{\rm v}{}^{-1}|\hat{H}_{\rm soc}|\psi_{\rm v}{}^{-1}\rangle\\ &=i\langle d_{xy}|\lambda\hat{L}_z|d_{x^2-y^2}\rangle-i\langle d_{x^2-y^2}|\lambda\hat{L}_z|d_{xy}\rangle=4\lambda\end{aligned} \tag{11}$$

When the magnetization direction is parallel to the x-axis, $\hat{H}_{\rm soc}=\lambda\hat{L}_x$, the valley of the valence band (conduction band) splits into $\Delta_{\rm CB}=\Delta_{\rm VB}=\langle\psi_{\rm v}{}^{1}|\lambda\hat{L}_x|\psi_{\rm v}{}^{1}\rangle-\langle\psi_{\rm v}{}^{-1}|\lambda\hat{L}_x|\psi_{\rm v}{}^{-1}\rangle=0$. The above analyses are consistent with our valley splitting results obtained from first principles calculations. The significant differences between valence band valley splitting and conduction band valley splitting are attributed to different basis functions determined by different orbital contributions of different K/$-K$ valleys.

For 2D hexagonal lattices, there may be anomalous Hall effects in the FVS materials without the assistance of a magnetic field. In the following, we will study the valley-related transport properties of the SVSiN$_2$ monolayer. The transport properties related to valleys are closely related to the Berry curvature. For a 2D system, the Berry curvature can be expressed as:

$$\Omega_z(k)=-\sum_{n}\sum_{n\neq n'}f_n\frac{2{\rm Im}\langle\psi_{nk}|v_x|\psi_{n'k}\rangle\langle\psi_{n'k}|v_y|\psi_{nk}\rangle}{\left(E_n-E_n'\right)^2} \tag{12}$$

where f_n is the equilibrium Fermi Dirac distribution function. ψ_{nk} and E_n is the Bloch wave function and its eigenvalues, respectively. v_x and v_y are the velocity operators along different

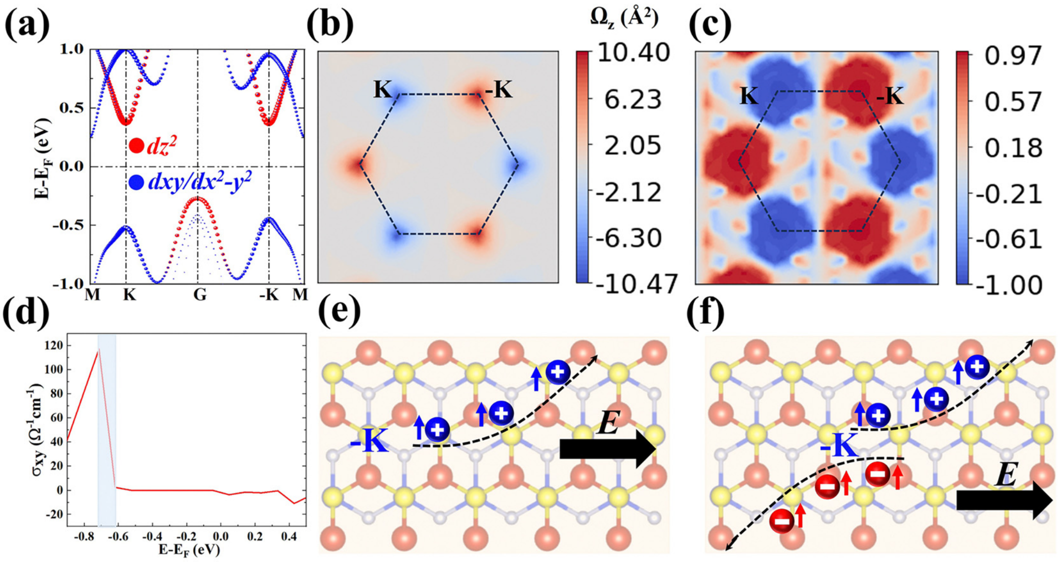

Fig. 5 The (a) orbital resolved electronic structure, (b) Berry curvature, (c) circular polarization, and (d) anomalous Hall conductivity of the SVSiN$_2$ monolayer. The Fermi level (E_F) is set to zero. (e) Schematic diagram of anomalous valley Hall effect under hole doping, with a V ion magnetic moment direction of +z. The blue arrow indicates the spin up state. (f) Schematic diagram of the anomalous valley Hall effect under specific frequency of right-handed circularly polarized light. Blue and red spheres represent hole and electron, respectively.

directions.[69,70] Here, the Berry curvature is obtained by summing all occupied states. Fig. S7 (ESI†) shows that the band structure based on the tight-binding model is consistent with the DFT results. From Fig. 5(b), it can be seen that the Berry curvature at the K and $-K$ valleys has opposite signs and different absolute values. Since the anomalous velocity $\upsilon \propto -\vec{E} \times \overrightarrow{\Omega_z}$, the non-zero and opposite Berry curvatures indicate that the SVSiN$_2$ monolayer exhibit opposite anomalous velocities at the $K/-K$ valleys. In contrast, the Berry curvature is close to zero at other positions in the momentum space. The anomalous Hall conductivity σ_{xy} can be calculated by integrating the Berry curvature over the whole occupied states:[71] $\sigma_{xy} = \frac{e^2}{h}\frac{1}{2\pi}\int_{BZ} d\mathbf{k}^2 \Omega(\mathbf{k})$. As shown in Fig. 5(d), the presence of AVHE is confirmed by the non-zero σ_{xy} highlighted by the shaded area. Furthermore, we have proposed a theoretical design to achieve AVHE, as shown in Fig. 5(e). Owing to the remarkable valley splitting of VBM at the $K/-K$ valleys, we can modulate the E_F to achieve hole doping at the desired valley, *e.g.*, the $-K$ valley shown in Fig. 4(c).

In addition, the non-zero berry curvature indicates that the $K/-K$ valley has chirality, in which the circularly polarized light selection rule can be described as:

$$\eta(\mathbf{k}) = \frac{|P_+(\mathbf{k})|^2 - |P_-(\mathbf{k})|^2}{|P_+(\mathbf{k})|^2 + |P_-(\mathbf{k})|^2} \tag{13}$$

where $P_\pm(k)$ represents the interband transition matrix.[72] As shown in Fig. 5(c), the left-handed (right-handed) circularly polarized light is related to the K ($-K$) valley.

Using a specific frequency of right circularly polarized light, an electron–hole pair with the same spin can be generated at the $-K$ valley, and the electron (hole) will accumulate at the top (bottom) of the sample, as shown in Fig. 5(f). The valley-contrasting transport properties are similar to those in the MoS$_2$ monolayer.[66]

3.4 Strain effects and topological phase transition

The exchange interaction in the SVSiN$_2$ monolayer is related to the overlap of orbital wave functions between ions. Therefore, the distance between magnetic ions or the distance (bond angle) between magnetic ions and ligand atoms, has a substantial impact on the electronic properties of the SVSiN$_2$ monolayer. Strain engineering has been widely used to modulate the electronic structure of 2D materials. One of the main advantages of 2D materials is that their tensile properties are much higher than their bulk counterparts.[73] Therefore, we examine the effect of biaxial strain within ±3% on the electronic structure of the SVSiN$_2$ monolayer. Here, the biaxial strain is simulated by changing the lattice constant of the crystal cell and can be defined as:

$$\varepsilon = \left(\frac{a - a_0}{a_0}\right) \times 100\% \tag{14}$$

where a_0 and a represents the lattice constants of the SVSiN$_2$ monolayer without and with biaxial strain, respectively. As shown in Fig. 6(a) and Fig. S8 (ESI†), both in-plane tensile and compressive strains tend to reduce the bandgap of the SVSiN$_2$ monolayer and maintain the characteristics of an indirect bandgap. Compared to the pristine SVSiN$_2$ monolayer, the CBM of the SVSiN$_2$ monolayer is shifted from the M-point to the $K/-K$ valley when an in-plane tensile strain is applied. Moreover, biaxial strains could tune the valley splitting of the SVSiN$_2$ monolayer, as shown in Fig. 6(d). It is found that when the strain is increased from −3% to 3%, the valley splitting of the valence band is linearly enhanced. We further plot the orbital resolved band structures of the SVSiN$_2$ monolayer under −3% and 3% biaxial strains, as shown in Fig. S9

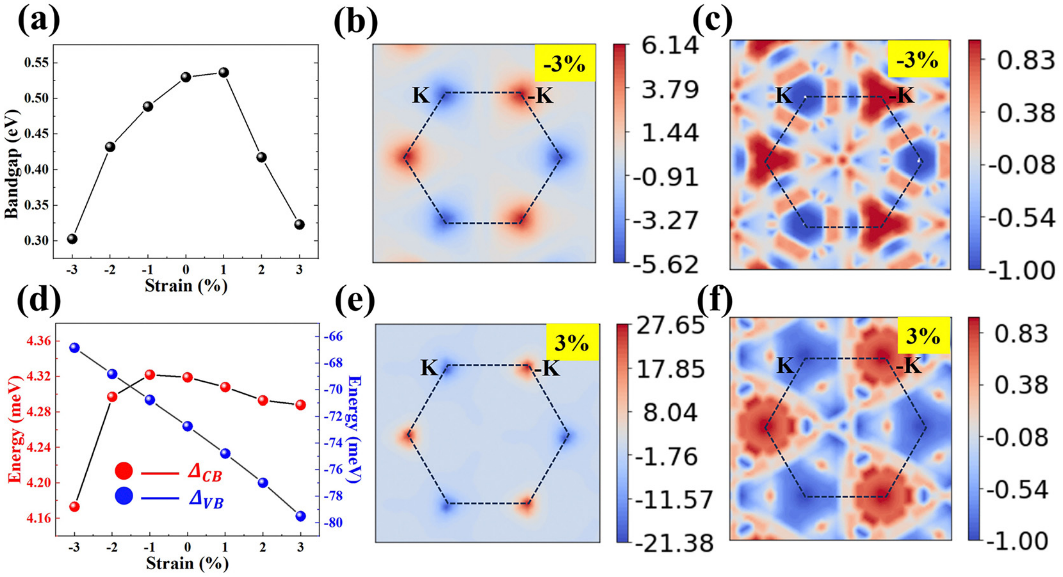

Fig. 6 (a) The bandgap of the SVSiN$_2$ monolayer under different strains. The Berry curvature distributions of the SVSiN$_2$ monolayer under (b) −3% and (e) 3% strain. The circular polarization of the SVSiN$_2$ monolayer under (c) −3% and (f) 3% strain. (d) The valley splitting for the conduction band Δ_{CB} (left column and red color online) and valence band Δ_{VB} (right column and blue color online) of the SVSiN$_2$ monolayer under different strains.

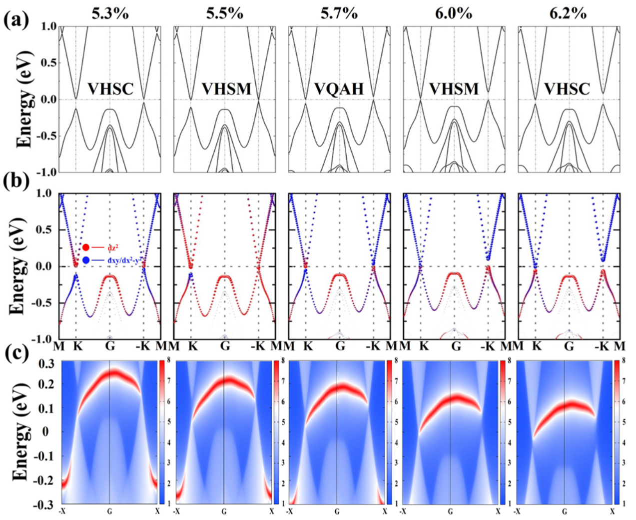

Fig. 7 The (a) band structure of the $SVSiN_2$ monolayer containing SOC under biaxial strain. The corresponding (b) orbital-resolved band structure and (c) edge state of the $SVSiN_2$ monolayer under biaxial strain.

(ESI†); the features of its conduction band at the *K*/−*K* valleys dominated by the d_{z^2} orbital, remains as the biaxial strain ranges from −3 to 3%. According to eqn (11), the valley splitting of the valence band remains a small value.

The in-plane biaxial strains give rise to the prominent influence on the Berry curvature at the *K*/−*K* valleys, as shown in Fig. 6(b) and (e). The variation of the Berry curvature at the *K*/−*K* valleys is consistent with the trend of valley splitting of the valence band, *i.e.*, a tensile strain induces a greater Berry curvature difference at the *K*/−*K* valleys. Furthermore, both the CBM and VBM at the *K*/−*K* valleys are shifted towards the E_F when a tensile strain is applied, as shown in Fig. S9 (ESI†). It is expected that the bandgap at the *K*/−*K* valleys could be closed when a sufficiently large strain is performed on the $SVSiN_2$ monolayer. Most importantly, the bandgap closure generally implies the presence of a strain-driven topological transition associated with a nontrivial electronic state.[74] We therefore calculate the orbital-resolved electronic structure and edge states of the SVSiN2 monolayer under 5.3–6.2% biaxial strain.

It can be seen from Fig. 7(a) and (b) that the $SVSiN_2$ monolayer is a valley-half-semiconductor (VHSC) when $\varepsilon < 5.5\%$. In contrast, the bandgap of the $SVSiN_2$ monolayer at the −*K* valley is essentially closed when a strain of $\varepsilon = 5.5\%$ is applied. Moreover, the VBM at the −*K* valley is contributed by the d_{z^2} orbital of the V atom, revealing the presence of strain-driven band inversion. Therefore, a valley-half-semimetal (VHSM) state is obtained under $\varepsilon = 5.5\%$. When the tensile strain is continuously increased, the bandgap at the −*K* valley reopens and the $SVSiN_2$ monolayer enters the valley quantum anonymous Hall (VQAH) state. When $\varepsilon = 6\%$, the bandgap of the $SVSiN_2$ monolayer at the *K* valley is closed, and a similar band inversion for the CBM is clearly observed at the *K* valley. Similar strain induced valley-dependent band inversion was also observed in the VSi_2N_4 monolayer and Janus $VSiGeN_4$ monolayer.[34,41,58] The band inversion is a strong implication of the nontrivial topological phase.[40,74] The bandgap at the *K* valley reopens and the $SVSiN_2$ monolayer becomes VHSC when $\varepsilon > 6\%$.

To understand the mechanism of multiple topological phase transitions, we analyzed the orbital projection band structure and edge states, as shown in Fig. 7(c). Under a tensile strain of 5.7%, it is found that an edge state crosses the Fermi level, and it connects the VBM at the *K* valley and the CBM at the −*K* valley. The strain induced edge state in the $SVSiN_2$ monolayer is very similar to the case of the strained (4.5–4.8%) $VSiCN_4$

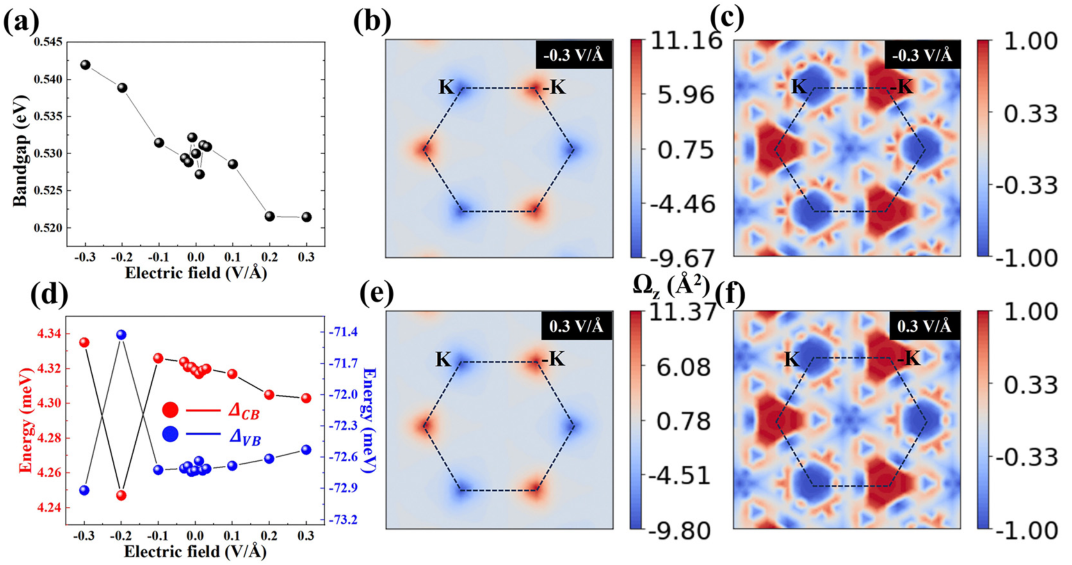

Fig. 8 (a) The bandgap of the $SVSiN_2$ monolayer under a vertical electric field. Berry curvature distributions of the $SVSiN_2$ monolayer under (b) −0.3 V Å^{-1} and (e) 0.3 V Å^{-1} vertical electric fields. The circular polarization of the $SVSiN_2$ monolayer under (c) −0.3 V Å^{-1} and (f) 0.3 V Å^{-1} vertical electric fields. (d) The valley splitting for the conduction band and valence band of the $SVSiN_2$ monolayer under different vertical electric fields.

monolayer.[41] The topologically nontrivial phase is characterized by the nonzero topology invariant. The Chern number $\mathbb{C}$ is obtained by integrating the Berry curvature in the first Brillouin zone, and the calculated $\mathbb{C}$ in the strain range 5.5–6% is -1. The nonzero topology invariant shows that the 5.5–6.0% strained $SVSiN_2$ monolayer possesses nonzero intrinsic quantum anomalous Hall conductivity σ_{xy} according to:[74]

$$\sigma_{xy} = -\mathbb{C}G_0 \tag{15}$$

where $G_0 = \frac{e^2}{h}$ is the quantum conductance. The VQAH is predicated to be achieved in the $SVSiN_2$ monolayer using a 6% in-plane tensile strain. The $SVSiN_2$ monolayer provides a new platform to explore valley-contrasting properties and strain-driven topological state transitions.

3.5 Effects of external electric field

In addition, we explore the effects of external electric field on the valleytronics properties of the $SVSiN_2$ monolayer, as shown in Fig. 8. The bandgap of the $SVSiN_2$ monolayer exhibits a decreasing trend in the range from negative electric field to positive electric field. Compared to the strain modulation, the vertical electric field gives rise to negligible influence on the bandgap variation, as confirmed in Fig. 8(a). Fig. S10 (ESI†) demonstrates that their band structures are almost unaffected by the electric field. The valleytronic properties of the $SVSiN_2$ monolayer are robust to the vertical electric fields. Therefore, the vertical electric field has a weak impact on the valley splitting and Berry curvature, as verified in Fig. 8(b)–(f). The different tuning behavior of biaxial strains and vertical electric fields on the $SVSiN_2$ monolayer enrich the understanding of its valley-dependent properties, and are helpful to the development of FVS devices.

4 Conclusions

Based on first-principles calculations, we have demonstrated that the $SVSiN_2$ monolayer is a promising FVS material. Our calculation results indicate that: (1) the $SVSiN_2$ monolayer is a 2D *XY* magnetic material with a Curie temperature of 260 K, and its in-plane magnetic anisotropy energy mainly originates from the hybridization of the p-orbitals, exhibiting excellent thermal and dynamical stability. (2) A giant valley polarization of -72.73 meV and opposite Berry curvatures can be achieved in the $SVSiN_2$ monolayer by shifting the magnetization from the in-plane to out-of-plane direction, leading to an anomalous valley Hall effect. (3) The valley-contrasting properties of the $SVSiN_2$ monolayer can be significantly tuned by in-plane biaxial strains. Specifically, the 5.5–6.0% strain driven topological phase transition is confirmed by the band inversion and nontrivial edge state. The calculated nonzero Chern number demonstrates that the strained $SVSiN_2$ monolayer possesses nonzero intrinsic quantum anomalous Hall conductivity to realize the valley polarized quantum anomalous Hall effect. (4) Compared to the in-plane strain modulation, the valley-related property of the $SVSiN_2$ monolayer is rather robust to the vertical electric fields. Overall, our research has broadened the scope of 2D FVS materials, which is beneficial for practical applications of the $SVSiN_2$ monolayer for valleytronic devices.

Conflicts of interest

The authors declare that they have no known competing financial interests or personal relationships that could have appeared to influence the work reported in this paper.

Acknowledgements

This work was supported by the National Natural Science Foundation of China (No. 62174088 and 62371238). We are grateful to the High-Performance Computing Centre of Nanjing University for providing the IBM Blade cluster system.

References

1 D. Xiao, W. Yao and Q. Niu, *Phys. Rev. Lett.*, 2007, **99**, 236809.
2 J. R. Schaibley, H. Yu, G. Clark, P. Rivera, J. S. Ross, K. L. Seyler, W. Yao and X. Xu, *Nat. Rev. Mater.*, 2016, **1**, 16055.
3 A. Rycerz, J. Tworzydlo and C. W. J. Beenakker, *Nat. Phys.*, 2007, **3**, 172–175.
4 H. Zeng, J. Dai, W. Yao, D. Xiao and X. Cui, *Nat. Nanotechnol.*, 2012, **7**, 490–493.
5 G. Aivazian, Z. Gong, A. M. Jones, R.-L. Chu, J. Yan, D. G. Mandrus, C. Zhang, D. Cobden, W. Yao and X. Xu, *Nat. Phys.*, 2015, **11**, 148–152.
6 K. F. Mak, K. He, J. Shan and T. F. Heinz, *Nat. Nanotechnol.*, 2012, **7**, 494–498.
7 A. Srivastava, M. Sidler, A. V. Allain, D. S. Lembke, A. Kis and A. Imamoglu, *Nat. Phys.*, 2015, **11**, 141–147.
8 D. MacNeill, C. Heikes, K. F. Mak, Z. Anderson, A. Kormányos, V. Zólyomi, J. Park and D. C. Ralph, *Phys. Rev. Lett.*, 2015, **114**, 037401.
9 P. Back, M. Sidler, O. Cotlet, A. Srivastava, N. Takemura, M. Kroner and A. Imamoğlu, *Phys. Rev. Lett.*, 2017, **118**, 237404.
10 R. Peng, Y. Ma, S. Zhang, B. Huang and Y. Dai, *J. Phys. Chem. Lett.*, 2018, **9**, 3612–3617.
11 J. Zhao, X. Jin, H. Zeng, C. Yao and G. Yan, *Appl. Phys. Lett.*, 2021, **119**, 213101.
12 W.-Y. Tong, S.-J. Gong, X. Wan and C.-G. Duan, *Nat. Commun.*, 2016, **7**, 13612.
13 Z. He, R. Peng, X. Feng, X. Xu, Y. Dai, B. Huang and Y. Ma, *Phys. Rev. B*, 2021, **104**, 075105.
14 H. Huan, Y. Xue, B. Zhao, G. Gao, H. Bao and Z. Yang, *Phys. Rev. B*, 2021, **104**, 165427.
15 H. Hu, W. Y. Tong, Y. H. Shen, X. Wan and C. G. Duan, *npj Quantum Mater.*, 2020, **6**, 7.
16 J. Liu, W.-J. Hou, C. Cheng, H.-X. Fu, J.-T. Sun and S. Meng, *J. Phys.: Condens. Matter*, 2017, **29**, 255501.

17 R. Peng, Y. Ma, X. Xu, Z. He, B. Huang and Y. Dai, *Phys. Rev. B*, 2020, **102**, 035412.
18 Y. Zang, Y. Ma, R. Peng, H. Wang, B. Huang and Y. Dai, *Nano Res.*, 2021, **14**, 834–839.
19 H.-X. Cheng, J. Zhou, W. Ji, Y.-N. Zhang and Y.-P. Feng, *Phys. Rev. B*, 2021, **103**, 125121.
20 S.-D. Guo, Y.-L. Tao, H.-T. Guo, Z.-Y. Zhao, B. Wang, G. Wang and X. Wang, *Phys. Rev. B*, 2023, **107**, 054414.
21 J.-D. Zheng, Y.-F. Zhao, Y.-F. Tan, Z. Guan, N. Zhong, F.-Y. Yue, P.-H. Xiang and C.-G. Duan, *J. Appl. Phys.*, 2022, **132**, 120902.
22 K. Sheng, B. Zhang, H.-K. Yuan and Z.-Y. Wang, *Phys. Rev. B*, 2022, **105**, 195312.
23 S.-D. Guo, Y.-L. Tao, G. Wang, S. Chen, D. Huang and Y. S. Ang, *Front. Phys.*, 2024, **19**, 23302.
24 W. Pan, *Phys. Rev. B*, 2022, **106**, 125122.
25 W. Zhou, G. Zheng, Z. Wan, T. Sun, A. Li and F. Ouyang, *Appl. Phys. Lett.*, 2023, **123**, 143101.
26 R. Li, N. Mao, X. Wu, B. Huang, Y. Dai and C. Niu, *Nano Lett.*, 2023, **23**, 91–97.
27 L. Cai, R. Li, X. Wu, B. Huang, Y. Dai and C. Niu, *Phys. Rev. B*, 2023, **107**, 245116.
28 Y.-L. Hong, Z. Liu, L. Wang, T. Zhou, W. Ma, C. Xu, S. Feng, L. Chen, M.-L. Chen, D.-M. Sun, X.-Q. Chen, H.-M. Cheng and W. Ren, *Science*, 2020, **369**, 670–674.
29 Q. Cui, Y. Zhu, J. Liang, P. Cui and H. Yang, *Phys. Rev. B*, 2021, **103**, 085421.
30 X. Feng, X. Xu, Z. He, R. Peng, Y. Dai, B. Huang and Y. Ma, *Phys. Rev. B*, 2021, **104**, 075421.
31 L. Yan, B.-T. Wang, X. Huang, Q. Li, K. Xue, J. Zhang, W. Ren and L. Zhou, *Nanoscale*, 2021, **13**, 18947–18954.
32 Y. Liu, Y. Ji and Y. Li, *J. Phys. Chem. Lett.*, 2021, **12**, 9149–9154.
33 Y. Feng, Z. Wang, X. Zuo and G. Gao, *Appl. Phys. Lett.*, 2022, **120**, 092405.
34 X. Zhou, R.-W. Zhang, Z. Zhang, W. Feng, Y. Mokrousov and Y. Yao, *npj Comput. Mater.*, 2021, **7**, 160.
35 Y. Qi, C. Yao, J. Zhao and H. Zeng, *Phys. Chem. Chem. Phys.*, 2023, **25**, 28104–28112.
36 J. Wang, Z. Zhang, J. Shen, M. Zhang, L. Niu and L. Bai, *J. Phys. Chem. C*, 2023, **127**, 18067–18075.
37 J. Zhao, Y. Qi, C. Yao and H. Zeng, *Phys. Rev. B*, 2024, **109**, 035408.
38 Y. Yin, Q. Gong, M. Yi and W. Guo, *Adv. Funct. Mater.*, 2023, **33**, 2214050.
39 C. C. Tho, S.-D. Guo, S.-J. Liang, W. L. Ong, C. S. Lau, L. Cao, G. Wang and Y. S. Ang, *Appl. Phys. Rev.*, 2023, **10**, 041307.
40 X.-S. Guo and S.-D. Guo, *Phys. Chem. Chem. Phys.*, 2023, **25**, 18577–18583.
41 P. Li, X. Yang, Q.-S. Jiang, Y.-Z. Wu and W. Xun, *Phys. Rev. Mater.*, 2023, **7**, 064002.
42 G. Kresse and J. Furthmüller, *Phys. Rev. B: Condens. Matter*, 1996, **54**, 11169–11186.
43 G. Kresse and J. Hafner, *Phys. Rev. B: Condens. Matter*, 1993, **47**, 558–561.
44 J. P. Perdew, K. Burke and M. Ernzerhof, *Phys. Rev. Lett.*, 1996, **77**, 3865–3868.
45 J. Heyd, G. E. Scuseria and M. Ernzerhof, *J. Chem. Phys.*, 2003, **118**, 8207–8215.
46 H. J. Monkhorst and J. D. Pack, *Phys. Rev. B: Solid State*, 1976, **13**, 5188–5192.
47 A. Togo and I. Tanaka, *Scr. Mater.*, 2015, **108**, 1–5.
48 S.-W. Kim, H.-J. Kim, S. Cheon and T.-H. Kim, *Phys. Rev. Lett.*, 2022, **128**, 046401.
49 N. Marzari, A. A. Mostofi, J. R. Yates, I. Souza and D. Vanderbilt, *Rev. Mod. Phys.*, 2012, **84**, 1419–1475.
50 Q. Wu, S. Zhang, H.-F. Song, M. Troyer and A. A. Soluyanov, *Comput. Phys. Commun.*, 2018, **224**, 405–416.
51 Y. Zhang, B. Wang, Y. Guo, Q. Li and J. Wang, *Comput. Mater. Sci.*, 2021, **197**, 110638.
52 K. Momma and F. Izumi, *J. Appl. Crystallogr.*, 2011, **44**, 1272–1276.
53 R. T. Sibatov, R. M. Meftakhutdinov and A. I. Kochaev, *Appl. Surf. Sci.*, 2022, **585**, 152465.
54 J. B. Goodenough, *Phys. Rev.*, 1955, **100**, 564–573.
55 J. Kanamori, *J. Phys. Chem. Solids*, 1959, **10**, 87–98.
56 D.-S. Wang, R. Wu and A. J. Freeman, *Phys. Rev. B: Condens. Matter*, 1993, **47**, 14932–14947.
57 C. Pellegrini, T. Müller, J. K. Dewhurst, S. Sharma, A. Sanna and E. K. U. Gross, *Phys. Rev. B*, 2020, **101**, 144401.
58 S.-D. Guo, W.-Q. Mu, J.-H. Wang, Y.-X. Yang, B. Wang and Y.-S. Ang, *Phys. Rev. B*, 2022, **106**, 064416.
59 D. Dey, A. Ray and L. Yu, *Phys. Rev. Mater.*, 2022, **6**, L061002.
60 K. Sheng, Q. Chen, H.-K. Yuan and Z.-Y. Wang, *Phys. Rev. B*, 2022, **105**, 075304.
61 J. L. Lado and J. Fernandez-Rossier, *2D Mater.*, 2017, **4**, 035002.
62 W.-B. Zhang, Q. Qu, P. Zhu and C.-H. Lam, *J. Mater. Chem. C*, 2015, **3**, 12457–12468.
63 H. Sun, S.-S. Li, W.-X. Ji and C.-W. Zhang, *Phys. Rev. B*, 2022, **105**, 195112.
64 Y. Qi, C. Yao, J. Zhao and H. Zeng, *Phys. Rev. B*, 2023, **108**, 125304.
65 Q. Li, C.-X. Zhang, D. Wang, K.-Q. Chen and L.-M. Tang, *Mater. Adv.*, 2022, **3**, 2927–2933.
66 D. Xiao, G.-B. Liu, W. Feng, X. Xu and W. Yao, *Phys. Rev. Lett.*, 2012, **108**, 196802.
67 D. Dai, H. Xiang and M.-H. Whangbo, *J. Comput. Chem.*, 2008, **29**, 2187–2209.
68 S. Konschuh, M. Gmitra and J. Fabian, *Phys. Rev. B: Condens. Matter Mater. Phys.*, 2010, **82**, 245412.
69 C. Ke, Y. Wu, W. Yang, Z. Wu, C. Zhang, X. Li and J. Kang, *Phys. Rev. B*, 2019, **100**, 195435.
70 Y. Yao, L. Kleinman, A. H. MacDonald, J. Sinova, T. Jungwirth, D.-S. Wang, E. Wang and Q. Niu, *Phys. Rev. Lett.*, 2004, **92**, 037204.
71 D. J. Thouless, M. Kohmoto, M. P. Nightingale and M. den Nijs, *Phys. Rev. Lett.*, 1982, **49**, 405–408.
72 T. Cao, G. Wang, W. Han, H. Ye, C. Zhu, J. Shi, Q. Niu, P. Tan, E. Wang, B. Liu and J. Feng, *Nat. Commun.*, 2012, **3**, 887.
73 L. Zhang, Y. Tang, A. R. Khan, M. M. Hasan, P. Wang, H. Yan, T. Yildirim, J. F. Torres, G. P. Neupane, Y. Zhang, Q. Li and Y. Lu, *Adv. Sci.*, 2020, **7**, 2002697.
74 X.-L. Qi and S.-C. Zhang, *Rev. Mod. Phys.*, 2011, **83**, 1057–1110.